Journal of Aerosol Science 121 (2018) 38–53

Contents lists available at ScienceDirect

Journal of Aerosol Science

journal homepage: www.elsevier.com/locate/jaerosci

Size-independent unipolar charging of nanoparticles at high concentrations using vapor condensation and its application for improving DMA size-selection efficiency

Yoohyun Ock[a], Jeonggeon Kim[a], Indae Choi[a,b], Dae Seong Kim[b], Mansoo Choi[b], Donggeun Lee[a,*]

[a] School of Mechanical Engineering, Pusan National University, Busan 46241, South Korea
[b] Department of Mechanical and Aerospace Engineering, Seoul National University, Seoul 08826, South Korea

ARTICLE INFO

Keywords:
Condensational growth
Nanoparticles
Size-independent charging
DMA
Monodispersity

ABSTRACT

The goal of this study was to achieve a significant improvement in the size-selection performance of DMA, by combining unipolar charging and the condensational method of growing nanoparticles. We developed a size-independent unipolar charger consisting of a saturator, a condenser, a corona charger, and an evaporator. Starting with a two-fluid mixing design, a porous-alumina-lined saturator was tested in terms of the size uniformity of particles after their condensational growth in a subsequent condenser. 20-nm Ag and 65-nm NaCl polydisperse nanoparticles were successfully grown into droplets of few micrometers with a geometric standard deviation of 1.20 or less. A simple model was also developed to explain the heat and mass transfer occurring in the saturator and condenser, resulting in predictions of particle growth that agreed with experimental results. The entire charging system was experimentally evaluated in terms of size dependencies of charging efficiency and charge numbers. The results revealed that ~52% of the nanoparticles were uniformly charged and released with a charge number of + 32, irrespective of the particle sizes. A regular nano DMA, using the proposed size-independent charging system in place of a bipolar charger, was finally tested to determine its productivity when size-classifying particles. It was found that the proposed charger, when combined with the DMA, was eight times more efficient compared to the bipolar charger, and became more advantageous as the target particle size decreased. These promising results were reconfirmed by TEM image analysis of the produced monodisperse particles.

1. Introduction

Nanoparticles have been widely used as key building blocks for renewable energy devices such as solar cells and fuel cells. Controlling the size of the nanoparticles during their production is important, since different particle sizes are often required depending on the application. For example, 2–10 nm Pt or 10–60 nm Au/Ag particles are recommended as catalysts for fuel cells or solar cells, respectively. Producing these nanoparticles with uniform size at high concentrations is crucial because the performance of the particles depends not only on their size but also on their size distribution. (Anantha, Cheng, Tay, Wong, & Ramanujan, 2015; Lee et al., 2014; Liu et al., 2006; Zeng et al., 2013)

The gas phase synthesis of nanoparticles provides one-step fabrication with easy scale-up for mass production compared to

* Corresponding author.
E-mail address: donglee@pusan.ac.kr (D. Lee).

https://doi.org/10.1016/j.jaerosci.2018.04.007
Received 30 January 2018; Received in revised form 20 April 2018; Accepted 26 April 2018
Available online 03 May 2018
0021-8502/

solution-based methods. However, the method is also known to be limited when it comes to precisely controlling the size monodispersity of the particles (Kruis, Fissan, & Peled, 1998; Lee & Choi, 2002; & Wang, Zhong, & Snyder, 1990). The objective of this study is to overcome the limitations of the method while retaining its strengths, i.e., producing monodisperse nanoparticles at high concentration. For this purpose, we employed a differential mobility analyzer (DMA) because it can classify nanoparticles by their size regardless of their chemical properties.

DMA basically utilizes differences in the electrical mobility of charged particles that occur as a result of their size (Hewitt, 1957; Knutson & Whitby, 1975). Because of the necessity of charging particles, an aerosol charger should always be installed prior to any types of DMA. The size-classifying performance of the DMA therefore relies heavily on the performance of the charger. A bipolar charger using a radioactive material (^{85}Kr, ^{210}Po, and ^{241}Am) or a soft X-ray generator has normally been used as the inlet charger of the DMA (Jiang et al., 2014). The size-dependent charge states of particles when bipolar chargers are used are well known. This is of primary importance for data conversion (Stolzenburg & McMurry, 2008) in a scanning mobility particle spectrometer (SMPS). DMA has mainly been used for measuring the size distribution of aerosol particles.

However, DMA is limited as a production tool for monodisperse nanoparticles because the charging efficiency (or charged fraction) of particles achieved with conventional bipolar chargers is unacceptably low when the particle size of interest goes below 30 nm (e.g., ~4% for 10 nm particles). In that size range, DMAs, including nano DMA, are also known to suffer from significant diffusion loss (Birmili et al., 1997; Chen et al., 1998; Kousaka, Okuyama, & Adachi, 1985) in addition to the inefficient charging problem.

Several approaches have been taken to increase the number concentration of DMA-selected monodisperse particles, for example, by operating the DMA at higher volume flowrates (Hontanon & Kruis, 2009) or modifying the DMA design to include three monodisperse outlets (Bezantakos, Giamarelou, Huang, Olfert, & Biskos, 2016). Although particle diffusion can be successfully suppressed by increasing the gas volume flow rates, the limited charging problem still remains.

In this respect, it is notable that unipolar corona chargers normally operate with much higher charging efficiencies due to the absence of charge recombination. For example, Domat, Kruis, and Fernandez-Diaz (2014)'s unipolar charger led to a ~40% charging efficiency at 10 nm, which is almost 10 times higher than that of the bipolar charger. This is an important strength. However, the method can introduce another problem, i.e., the multiple charging of nanoparticles. When singly-charged small particles coexist with multiply-charged large particles, the two different types of particles can have identical electrical mobility and be classified simultaneously by a DMA, resulting in a significant deterioration in the monodispersity of DMA-selected particles. To address this problem, many efforts have been made to reduce the fraction of multiply charged particles, by optimizing a key parameter (the $N_i t$ product) of diffusion charging (Vivas, Hontanon, & Schmidt-Ott, 2008), or utilizing a tandem-DMA (TDMA) setup (Lüönd & Schlatter, 2013; Yook et al., 2008).

Trials utilizing unipolar chargers have been successful for measuring the size distribution of nanoparticles. However, efforts with unipolar chargers always entail a significant reduction in the yield of monodisperse particles. This is mainly because the number of charges that the particles achieve in the unipolar chargers is strongly and inevitably dependent on the size of the particles, besides the fact that their charging efficiency is likewise size-dependent (Domat et al., 2014; Vivas et al., 2008). There is a strong need for an ideal charger capable of size-independent charging of any nanoparticle with high efficiency, and this has motivated the present study.

The key idea in this study is to combine the condensational growth of nanoparticles and unipolar charging. The growth rate of a particle by vapor condensation is inversely proportional to particle diameter (d_p) as shown in Eq. (1):

$$\frac{d(d_p)}{dt} = \frac{4MD_v}{R\rho_p d_p}\left(\frac{P_\infty}{T} - \frac{P_d}{T}\right) \approx \frac{4MD_v P_d}{R\rho_p T d_p}(S-1) \propto \frac{1}{d_p}, \tag{1}$$

where M is the molecular weight of a condensing vapor, ρ_p is the liquid-phase density of the vapor, D_v is the diffusion coefficient of the vapor, R is the gas constant, P_∞ is the partial pressure of the vapor near the particle, P_d and T_d are the vapor pressure and temperature on the surface of the growing particle respectively, T is the temperature of the surrounding vapor phase, and S is the supersaturation ratio of the vapor. (Hinds, 1999) Since the growth rate of small particles is higher than that of larger particles during condensational growth, the small particles can catch up with the larger ones in size, which makes the size distribution of growing particles narrower with time, becoming nearly monodisperse in size. At the same time, if the nanoparticles are grown into monodisperse microdroplets ahead of a unipolar charger, more efficient unipolar charging of nanoparticles is expected to occur, nearly independent of their original sizes. Finally, these charges are retained on the nanoparticles after the condensed liquid is evaporated from the droplets, which enables this method to resolve the two problems, i.e., the size-dependency of the unipolar charger and the low charging efficiency of the bipolar charger, at the same time.

To date, there have been only a few reports on the subject of increasing charging efficiency using the condensational growth of nanoparticles. (Choi & Kim, 2007; Kim, Lee, Woo, & Choi, 2006; Suh, Han, Kim, & Choi, 2005). The first two papers reported that mean charging efficiency and the number of charges of particles were greatly enhanced by applying a corona diffusion charger to coarse droplets grown by vapor condensation, however the number of charges widely varied in a range from 10 to 71 depending on the sizes of the original particles (12–29 nm, respectively). This conversely means that precise control of the supersaturation state of the vapor leading to particle growth is not practically easy. To the best of our knowledge, there is only one paper that experimentally demonstrated the size-independent unipolar charging of nanoparticles using vapor condensation (Choi & Kim, 2007). It is however noted that their experiments were done only for DMA-selected monodisperse particles at low concentrations. It is not yet certain whether their approach works for size-polydisperse nanoparticles at high concentrations or not. In addition, there is still no evidence that the size-classification performance of a DMA could practically be improved by using the size-independent unipolar charger in

place of a bipolar charger.

The objective of this study is therefore to clarify these two unknowns by experiments. A porous alumina-lined saturator was developed starting with a two-fluid mixing saturator, and installed ahead of a cool condenser where particles are supposed to grow by condensation of supersaturated ethylene glycol (EG) vapor. Since the monodispersity of the grown droplets exiting the condenser directly determines the size independency of the succeeding corona charger, changes in the size and geometric standard deviation (GSD) of particles before and after their condensational growth were monitored with great care at different concentrations of particles.

Two types of polydisperse aerosol particles (NaCl and Ag) were successfully grown, with a considerable decrease in GSD, and their size-independent unipolar charging was experimentally verified. A simple numerical model was also developed to explain the significance of the design parameters of the saturator and condenser. Lastly, by replacing the bipolar charger with our size-independent charger upstream of the DMA, its size-classification performance was tested, utilizing a TDMA system. Then the size distribution of the first DMA-selected Ag particles was compared with that of the bipolar charger. The first DMA-selected particles, after being deposited on a TEM grid, were imaged by transmission electron microscope (TEM) and the resulting size distribution was determined to be in a reasonable agreement with the results of the TDMA.

2. Methods and design concept

2.1. Synthesis of aerosol nanoparticles at high concentrations

In order to produce monodisperse nanoparticles for electrostatic classification at high concentrations, it is essential to first generate nanoparticles at high concentrations, which was achieved using two different kinds of nanoparticle generators. First, polydisperse Ag nanoparticles with a GMD of 20 nm at a total concentration of $\sim 10^5$ # cm^{-3} were produced through fast evaporation and condensation of a Ag pellet using a home-made spark discharger (Lee et al., 2011). Second, polydisperse NaCl nanoparticles with a GMD of 60–70 nm at a total concentration of $\sim 10^4$ # cm^{-3} were produced by a spray-drying method (Lee, Park, & Zachariah, 2005; Pyo, Ock, Jeong, Park, & Lee, 2017).

The carrier gas N_2 was used to deliver the two types of particles into a saturator-condenser assembly (which will be called a particle magnifier) for the growth of the particles. In particular, NaCl particles with a wider size distribution were classified into 20, 30, and 40 nm by a DMA to further assess the charging characteristics of our size-independent unipolar charger as a function of particle size. The smaller Ag nanoparticles at the highest concentration were used to assess the size classification performance of the present charger-installed nano DMA at 14.5 nm in diameter.

Since some of those (particularly Ag) nanoparticles could be charged to some extent during the synthesis process, the charged fraction of particles was eliminated by a 5-kV electrostatic precipitator (EP1) so that only uncharged particles enter the particle magnifier (refer to Fig. 1). The total number concentration (N_{t0}) and size distribution of the uncharged particles were measured by a condensation particle counter (CPC; TSI 3025A) and a scanning mobility particle sizer (SMPS).

2.2. Size-independent charging

Fig. 1 shows a schematic diagram of the experimental setup developed in this study. The size-independent charger developed in this study, marked by a dashed line in the figure, consists of a particle magnifier combining a saturator and a condenser, a corona unipolar charger, and an evaporator. In this section, the key components are described in the order of sequence, as follows.

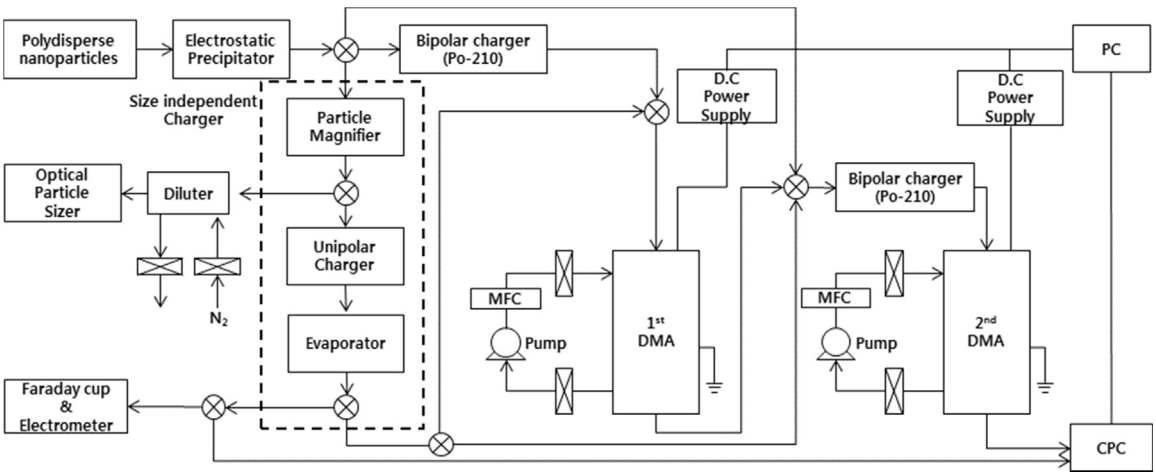

Fig. 1. Schematic drawing of the newly developed size-independent unipolar charger, and the measurement devices used to produce size-monodisperse nanoparticles at high concentration.

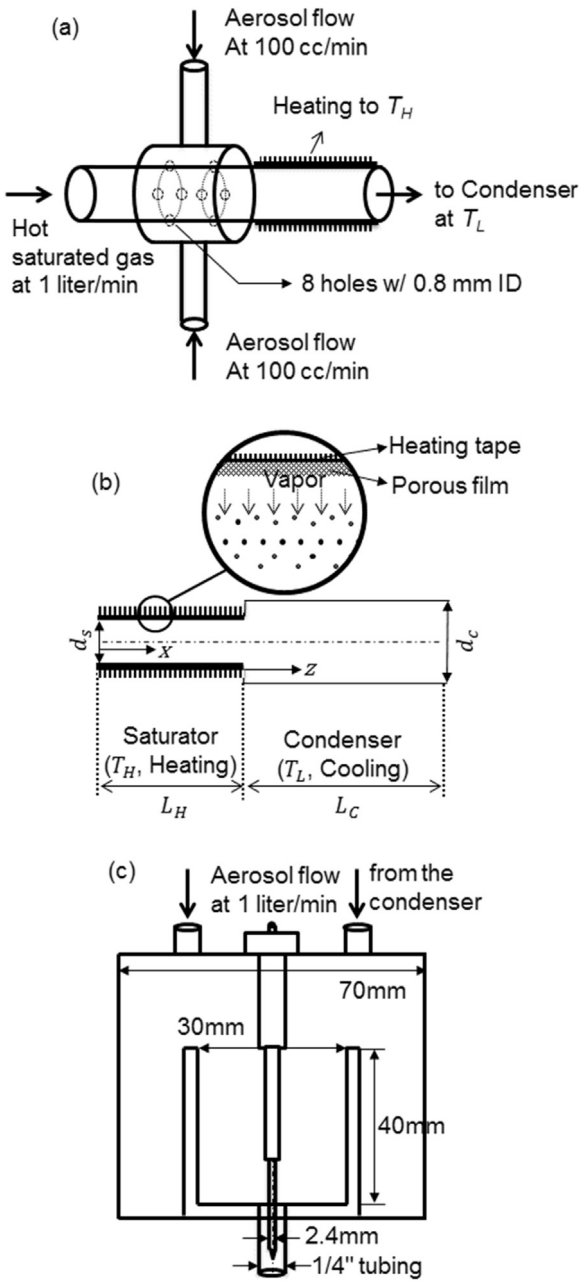

Fig. 2. Schematic drawings of two types of saturators connected with a condensing tube and a subsequent pin-cup corona charger: (a) a two fluids-mixing type saturator where an aerosol flow is mixed with a saturated gas, (b) a porous alumina-film lined saturator where EG liquid evaporates through the porous lining to saturate the incoming aerosol flow, (c) a home-made pin-cup corona charger where a high voltage is given to the central pin and the metallic cup is grounded.

First, two different types of saturators were considered in this study. Fig. 2(a) shows the first type, i.e., a two fluid-mixing saturator where a hot humid gas is mixed with an aerosol flow and then slightly heated again to reach the saturator temperature (T_H). As an example, an aerosol flow of 100 ccm at 20 °C was mixed with a saturated N_2 flow of 1000 ccm at 60 °C, leading to a mixed gas with a supersaturation ratio of 1.16 at 56 °C. The mixed gas was slightly heated to 59 °C to achieve a near-saturation state and then was fed into a ½″ diameter condensing tube at 20 °C. Ethylene glycol (EG) was employed as a condensing vapor; the reason for this choice will be explained in Appendix A. Note that in this type of saturator, aerosol particle flow is inevitably diluted by the mixing gas, leading to a decrease in the yield of monodisperse particles.

The second type of saturator was designed to improve the disadvantages of the first design. For that purpose, a single saturating tube whose inner surface was lined with a porous alumina was employed, as shown in Fig. 2(b). The EG liquid was provided through

the pore spaces in the alumina and evaporated to saturate the aerosol flow. The outer wall of the saturating tube was electrically heated by a heating wire so that the saturator temperature (T_H), defined as the wall temperature at the exit of the tube, was controlled in a range of 40–80 °C. A 30-cm long cylindrical tube with a ½" outer diameter (ID = 1.04 cm) was considered first in the second type of saturator, then a larger tube with OD = 1″ (ID = 2.24 cm) was tested later.

The end of the saturating tube was connected to a 70-cm long cylindrical tube whose outer surface was simply exposed to the room air for natural cooling without any coolant. For simplicity, the room temperature (20 °C) was defined as the condenser temperature (T_L). The outer diameter of the condensing tube was initially ½″ (ID = 1.04 cm) but was later reduced to ¼″(ID = 0.48 cm).

The incoming EG vapor becomes supersaturated in the condenser by cooling and is condensed onto the particle surfaces, encapsulating the particle with EG liquid in the form of a droplet. The size distributions of the droplets containing nanoparticles were measured using an optical particle sizer (OPS 3330, TSI co.) with particular focus on the variations in their GSDs. The saturator-condenser assembly in this study is called the 'particle magnifier'.

The droplets were then fed to a home-made pin-cup corona unipolar charger (see Fig. 2(c)) and charged to higher charge levels with higher efficiencies as expected by their enlarged sizes (Kim et al., 2006; Suh et al., 2005). If polydisperse particles grew to a single size by condensation, the charge numbers of the grown droplets converge into a single value regardless of the initial sizes of the particles.

Next, the condensed liquid on the droplets was evaporated and eliminated by an evaporator consisting of a tube furnace (at 400 °C) and a diffusion dryer with activated carbon. After evaporation of the EG, the particles return to their original state while maintaining the charge. Highly effective and size-independent charging can be achieved in this way. Note that all of the system components in the present charger were straight and connected each other without any bends in the tubing, to minimize particle loss.

In order to confirm the particles returned to their original state following evaporation, the total number concentration (N_t) and the size distribution of the particles were measured downstream of the evaporator by a CPC and a bipolar charger-installed SMPS, respectively, and compared with those of the original particles, to assess whether there was any particle transport loss through the size-independent charger.

Charged particles exiting the evaporator were removed by a subsequent 6-kV electrostatic precipitator (called 'EP2'), while the uncharged ones passed through the EP2. The difference in number concentration of the particles downstream of the EP2 was monitored by switching the EP2 on and off, yielding the extrinsic charging efficiency (η_c) of the present charger, using Eq. (2):

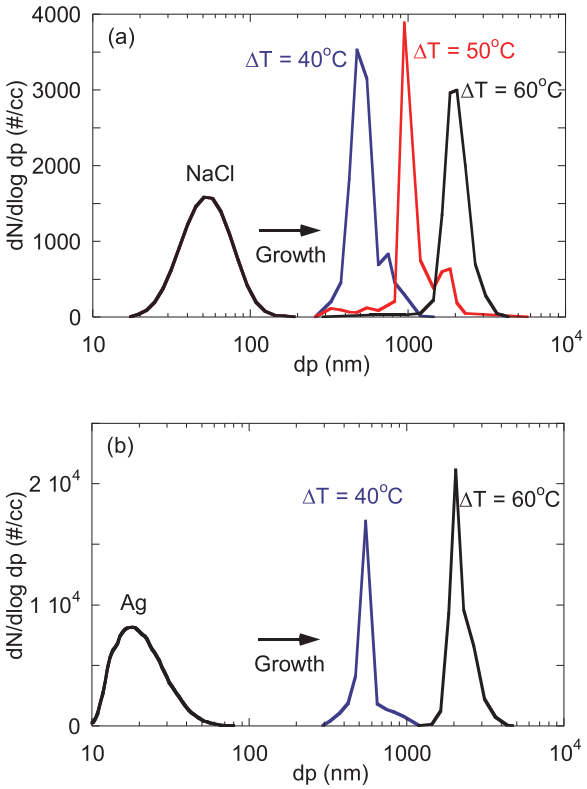

Fig. 3. Condensational growth of (a) inorganic NaCl and (b) metallic Ag nanoparticles with the two fluids-mixing type saturator and condensing tube; for NaCl particles, Q_p = 100 ccm & Q_{EG} = 500 ccm, whereas for Ag particles, Q_p = 10 ccm & Q_{EG} = 800 ccm. ΔT represents the temperature difference between the saturator and the condenser. The size distributions of the two pristine particles were measured in a dry condition, by flowing dry nitrogen gas with the same volume flow rates in place of the saturated gas.

$$\eta_c = \frac{N_c}{N_{t0}} = \frac{N_t - N_{nc}}{N_{t0}}, \tag{2}$$

where N_c and N_{nc} represent the total number concentrations of charged and uncharged particles by the present charger, respectively, whereas N_{t0} indicates the number concentration of the original particles.

After measuring the charge current (I) of the particles by Faraday cup and Keithley 6430 Electrometer at the end of the evaporator, the charge number (n_c) of the particles was calculated based on the value of N_c as seen in Eq. (3).

$$n_c = \frac{I}{N_c Q e}, \tag{3}$$

where Q is the flow rate of the carrier gas and e is the elemental charge (1.6×10^{-19} C). In this way, the performance of the size-independent charger was investigated in terms of η_c and n_c for three different sizes of NaCl particles.

2.3. Classification of monodisperse nanoparticles at high concentrations

The size classification for polydisperse NaCl and Ag particles was carried out using a long DMA (TSI 3081) or a nano DMA (TSI 3085) with either the developed size-independent unipolar charger or a conventional bipolar charger (^{210}Po). With the proposed charger, the high voltage used to operate the first DMA was appropriately reduced, based on the mean charge number of the particles. The size distributions of the monodisperse particles classified as such with the DMA were measured with a subsequent SMPS employing a bipolar charger, and the results were compared with each other to assess improvement in the size classification performance. The first and the second DMAs were operated in tandem with a sheath to aerosol flow ratio of 10:1 (Rader & McMurry, 1986). In addition, the classified particles from the proposed charger were captured on a TEM grid, and their size distribution was determined by TEM image analysis. The results were also compared with the corresponding TDMA result to reconfirm the size uniformity.

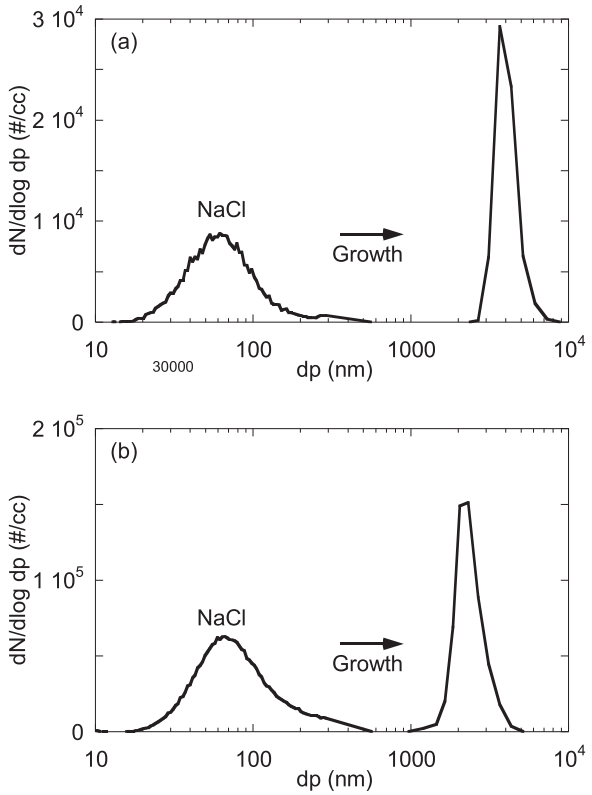

Fig. 4. Condensational growth of inorganic NaCl nanoparticles with the alumina-lined saturator and condensing tube ($d_s = d_c = ½''$); $T_H = 45$ °C, $T_L = 20$ °C, $Q_p = 500$ ccm (a) at a low concentration and (b) at a high concentration.

3. Results and discussion

3.1. Condensational growth of nanoparticles using a two-fluid mixing saturator and a condenser tube

Fig. 3(a) shows the size distribution of the NaCl nanoparticles before and after passing through the particle magnifier consisting of the mixing type of saturator illustrated in Fig. 2(a) and a condenser tube. The NaCl nanoparticles having a GMD of 46 nm and a GSD of 1.55 grew to 0.5, 1.0, 2.0 μm in GMD when the temperature difference ΔT increased ($= T_H - T_L$) to 40, 50, 60 °C, respectively. At the same time, their GSD decreased to 1.25, 1.36, 1.30, respectively, relative to the initial value of 1.55. However, the GSD never decreased below 1.25, but rather was scattered around 1.30. Note that the size distribution profiles of ΔT = 50 °C and 60 °C denote a small shoulder.

These seemingly bimodal size distributions suggest that the particles are grown by two different pathways. When the aerosol flow at Q_p = 100 ccm is injected through the circumferential holes into the saturated hot gas at Q_{EG} = 500 ccm, the aerosol particles are likely pushed outward to the tube surface. Particularly if the axysymmetry between eight radial inward jets is not perfect, the particles can take different routes in a spatially non-uniform gas mixture, so that their size distribution is possibly either broadened or bimodal.

This experiment was repeated for smaller Ag nanoparticles with a GMD of 20.4 nm and a GSD of 1.45, adjusting the gas flow rates to Q_p = 10 ccm and Q_{EG} = 800 ccm in an attempt to alleviate the non-uniformity of the gas mixture. Fig. 3(b) shows that the Ag nanoparticles were successfully grown to over 1 μm, while the GSD decreased to 1.24 and 1.19 as the ΔT increased to 40 and 60 °C, respectively. However, it should be noted that such a high ratio of gas mixing leads to an excessive dilution of aerosol flow, eventually lowering the concentration of monodisperse particles, as described earlier.

3.2. Condensational growth of nanoparticles using a porous alumina-lined saturator and a condenser tube

To avoid the abovementioned dilution problem in the saturator, a second type of saturator employing a porous alumina lining (see Fig. 2(b)) was developed and tested with the condenser tube. A similar experiment of condensational growth was performed with a 30-cm long alumina-lined saturator with d_s = ½" (ID 1.04 cm) and a 70-cm long condenser with d_c = ½". Regarding the success in Fig. 3(b) where the aerosol particles were diluted by the saturated gas, ten-times diluted NaCl nanoparticles with N_{to} = 4400 # cm^{-3} were first used for the test.

Fig. 4(a) shows that NaCl nanoparticles with a GMD of 62 nm and a GSD of 1.64 were successfully grown to microdroplets with a GMD of 4.0 μm and a GSD of 1.17 under conditions of T_H = 45 °C and T_L = 20 °C. Note that total number concentration of the microdroplets was ~4390 # cm^{-3}, which implies that the transport loss of particles through the entire particle magnifier was negligible, within 1%. This experiment was repeated for undiluted NaCl nanoparticles with N_{to} = ~34,640 # cm^{-3}. Fig. 4(b) shows that undiluted NaCl nanoparticles with a GMD of 75 nm and a GSD of 1.72 were grown to microdroplets with a GMD of 2.03 μm and a GSD of 1.23. In comparison with the low-concentration case in Fig. 4(a), the microdroplets have a smaller GMD and slightly larger GSD at the higher concentration.

This seems to indicate that the nanoparticles underwent insufficient condensational growth, probably because the per-particle concentration of supersaturated EG vapor was too low to grow ten-times more nanoparticles. Given the increase in GMD with condensation, the volume flow rate of the carrier gas (Q_p), and N_{to}, the required supply rate of EG for growing nanoparticles to the droplet size was calculated to be 1.18 × 10^{-6} g s^{-1}. This required value is an order of magnitude lower than the maximum supply rate of EG (1.25 ×10^{-5} g s^{-1}) that can be attained assuming complete saturation at the saturator outlet. Thus, the amount of EG vapor around the particles is not likely deficient on average (this will be discussed in the next section).

Another possible explanation is that the nanoparticles, upon entering the condenser, can experience different temperature-concentration paths depending on their radial positions at the inlet, which leads to variation in the sizes of particles after growth, thus

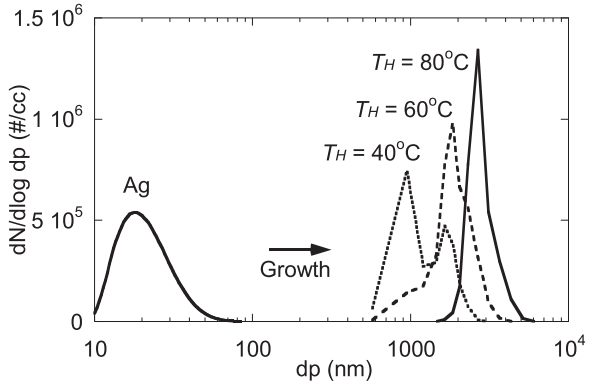

Fig. 5. Condensational growth of metallic Ag nanoparticles at the highest concentration with the alumina-lined saturator and condensing tube (d_s = 1", d_c = ¼"); T_H = 40, 60, 80 °C, T_L = 20 °C, Q_p = 500 ccm.

broadening their size distributions. At the entrance region of the condenser ($z \leq 0.1$ m), while the T_m of gas sharply decreases with z along the tube, EG vapor is consumed by the particle growth and the diffusion loss to the wall. Basically, the EG vapor is subject to higher radial concentration gradients near the wall compared to the near-axis region. Thus, the EG vapor is likely more quickly consumed near the wall. As a result, particles passing through the wall region may not grow as much as those near the axis, which can cause broadening in the size distribution of particles. This limited growth of particles near the wall is likely aggravated when there are more particles.

To address these two speculative problems, the saturator-condenser design was changed, by doubling the diameter of the saturator and halving the diameter of the condenser ($d_s = 1''$ and $d_c = ¼''$). The abrupt narrowing of the flow path at the inlet of the condenser might produce a radially inward force so that the particles move toward the central axis from the wall (Lee, Hwang, Kim, Kim, & Lee, 2013). In addition, the enlarged saturator was thought to provide a larger area for evaporation of the EG, and the saturator temperature (T_H) was also increased up to 80 °C to compensate for the shortened residence time of the particles in the narrowed condenser.

Fig. 5 demonstrates that this approach works, and that smaller Ag nanoparticles were successfully grown even at the highest number concentration ($\sim 2 \times 10^5$ # cm^{-3}). As the T_H increases from 40 to 60 and 80 °C, the 20.4-nm nanoparticles with a GSD of 1.45 grew into microdroplets whose GSD decreased from 1.48 to 1.37 and finally 1.20, respectively. The total number concentration of microdroplets was almost invariant within 5% with increasing T_H, suggesting that the transport (either diffusive or thermophoretic) loss of particles through the particle magnifier is acceptable.

3.3. Understanding condensational growth in a saturator and a condenser

The model described in Appendix B was used to analyze heat and mass transfer and the resulting particle growth in the particle magnifier, and the prediction results were compared with experimental data, as shown in Figs. 4 and 5. First, for the saturator with $d_s = ½''$ at $T_H = 45$ °C, the mean temperature of the gas (T_m), wall temperature ($T_{w,s}$), mean partial pressure (P_m) of EG and its saturation vapor pressure at the wall (P_w) were calculated as a function of z under a uniform heat flux condition (the constant q_s''). Fig. 6(a) shows that T_m linearly increases through the entire saturator and $T_{w,s}$ increases in parallel with the T_m. Recalling Eqs. (B2 and B3), this suggests that the gas flow becomes thermally fully developed, and $h_{i,s}$ becomes constant. (Incropera, Dewitt, Bergman, & Lavine, 2007) The $T_{w,s}$ reaches the target temperature ($T_H = 45$ °C) at the outlet ($z = 0.3$ m). It should be noted that not as much wall-to-gas mass transfer of EG occurs as expected; P_m at $z = 0.3$ is only 40 Pa, i.e., two thirds of P_w (64 Pa) at the target temperature, indicating that the gas was undersaturated at the outlet. Based on this data, the real supply rate of EG vapor from this saturator was calculated to be 8.93×10^{-6} g s^{-1}. This is still much larger than the value (1.18×10^{-6} g s^{-1}) required for the growth of the low-concentration NaCl particles in Fig. 4(a), but slightly lower than that (9.34×10^{-6} g s^{-1}) used to grow the high-concentration NaCl particles in Fig. 4(b).

Fig. 6(b) shows profiles of the temperatures and vapor pressures as a function of z from the inlet of the condenser ($d_c = ½''$ and $T_L = 20$ °C). It is worth noting that the wall temperature of the condenser ($T_{w,c}$) is not the same as the T_L but gradually decreases along the tube, approaching the surrounding temperature ($T_\infty = T_L = 20$ °C) at around $z = 0.2$ m. This is mainly due to inefficient natural convective cooling on the outer surface of the condenser. The model calculation confirms that the $T_{w,c}$ decreases almost instantaneously to T_L when the condenser is cooled by flowing water (e.g., by applying a typical value of 100 W m^{-2} K^{-1} for $h_{o,c}$ in Eq. (B7)). Here, the T_m catches up with the decreasing $T_{w,c}$ in $0.1 \leq z \leq 0.2$, which occurs much faster than the P_m of the EG vapor decreases. The P_m still holds up above P_w until $z = 0.3$, though the P_w decreases as fast as T_w because of its temperature-sensitive nature. This is attributed to the fact that the mass diffusivity of EG ($D_{EG} = 3.6 \times 10^{-6}$ m^2 s^{-1}) is lower than the thermal diffusivity of gas ($\alpha = 2.7 \times 10^{-5}$ m^2 s^{-1}) as stated in Appendix A.

Fig. 6(c) shows the axial profiles of the supersaturation ratio (S) and the diameter (d_p) of the growing microdroplets on average. Recalling Eq. (B10) and the relevant assumption, the vapor pressure difference of ($P_m - P_d$) or ($P_m - P_{sat}(T_m)$), also defined as $P_m(S - 1)$, was a driving force for the condensational growth. In response to the profiles of P_m and T_m in Fig. 6(b), the S quickly increases initially and reaches a maximum of 1.8 at $z = \sim 0.1$, and then decreases again with z. It is notable that the S remained above 1.0 up to $z = 0.5$, causing the particles to keep growing throughout the condenser.

The final diameter attained by the microdroplets at $z = 0.7$ was predicted to be 3.8 μm, which is in good agreement with the experimental data (~4 μm of GMD in Fig. 4(a)). Also note that the S begins to go beyond 1.0 only when $z \geq 0.014$, as if the condensation requires a sort of short latency period. For $z \leq 0.014$, in contrast, the P_m is temporarily lower than the vapor pressure on the particle surface $P_{sat}(T_m)$. The reversal of these pressures would never happen under water cooling of the condenser. This was observed only in the short entrance region where the condenser wall is still warm (e.g., $T_{w,c} \geq 31.1$ °C) which slows down the cooling of the gas to $T_m \geq 38.7$ °C. Thus, the nanoparticles, which are essentially non-volatile, were assumed to maintain their initial diameters in the region ($S \leq 1$).

The model calculations were repeated for the Ag nanoparticles at $\sim 2 \times 10^5$ # cm^{-3}, using the second design of the particle magnifier with $d_s = 1''$ and $d_c = ¼''$ (called Saturator 2 and Condenser 2 in Fig. 7) under the conditions shown in Fig. 5 ($T_H = 80$ °C). As shown in Fig. 7, the overall profiles of temperatures, vapor pressures, and particle sizes obtained for this design are apparently similar to those in Fig. 6. Fig. 7(a) shows that the wall temperature ($T_{w,c}$) reaches the target temperature, 80 °C at the exit of the saturator as expected, increasing the P_w to 700 Pa. It is however noted that the P_m is far smaller than the P_w, suggesting that the enlarged saturator is not as efficient at saturating the gas. In other words, the gas leaving Saturator 2 is relatively dry in comparison with Saturator 1, though the absolute value of P_m is three times higher. Nevertheless, the supply rate of EG vapor (2.9×10^{-5} g s^{-1}) estimated based on these data is high enough on average to make the Ag particles grow to 2.8 μm, as shown in Fig. 5 because the

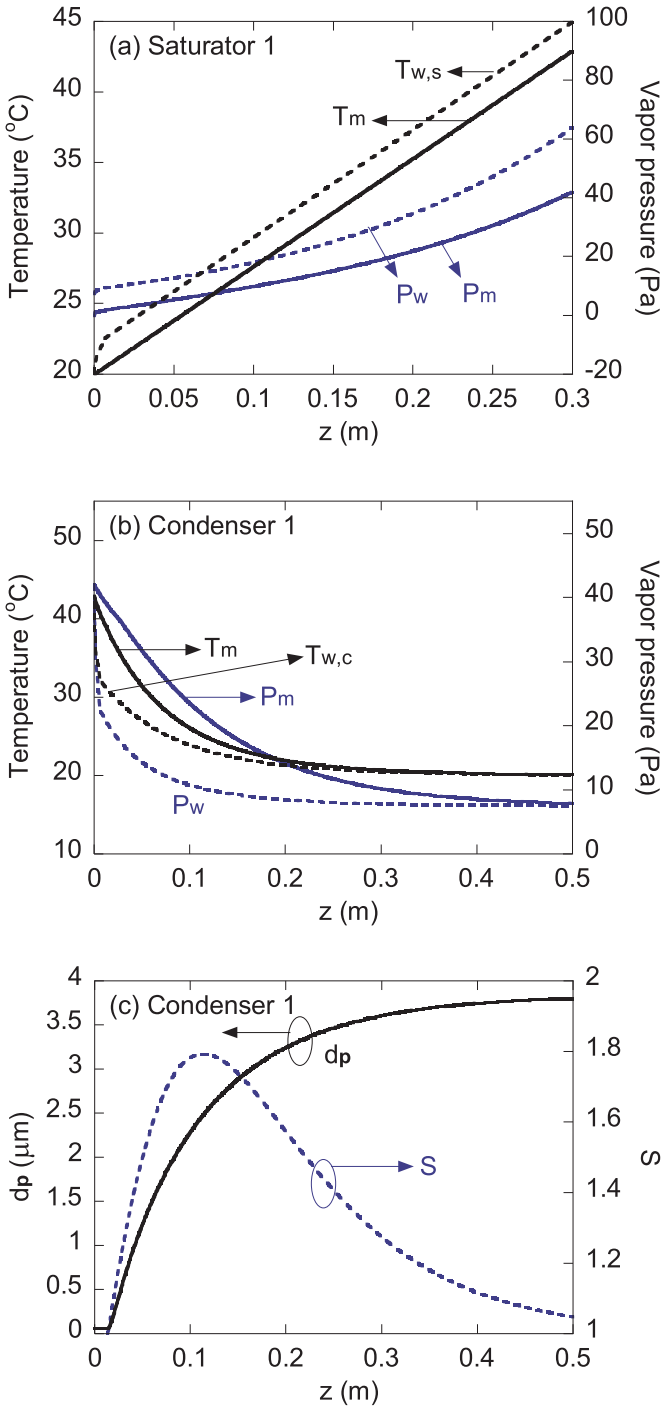

Fig. 6. Model predictions of axial profiles of (a) temperatures of gas and vapor pressures of the EG vapor in Saturator 1 (d_s = ½"), (b) temperatures of gas and vapor pressures of EG vapor in Condenser 1 (d_c = ½"), (c) supersaturation ratio of EG vapor and diameters of growing particles in Condenser 1; T_H = 45 °C, T_L = 20 °C, Q_p = 500 ccm.

required feeding rate of EG is 2.1×10^{-5} g s^{-1}.

In Fig. 7(b), the decreasing patterns of temperatures and vapor pressures are similar to those in Fig. 6(b). Based on these data, in Fig. 7(c), the aforementioned latency period where S ≤ 1.0 was remarkably elongated up to z = 0.045. In addition, the profile of S seems to be shifted to the downstream in response to the increase in gas velocity through the narrowed condenser. The maximum S was 2.57 at z = 0.17, while the maximum (1.79) was at z = 0.11 in Fig. 6(c). Despite the higher heating temperature, which led to the higher supersaturation ratio S in Saturator 2, the predicted diameter of the microdroplets at the exit of Condenser 2 was only

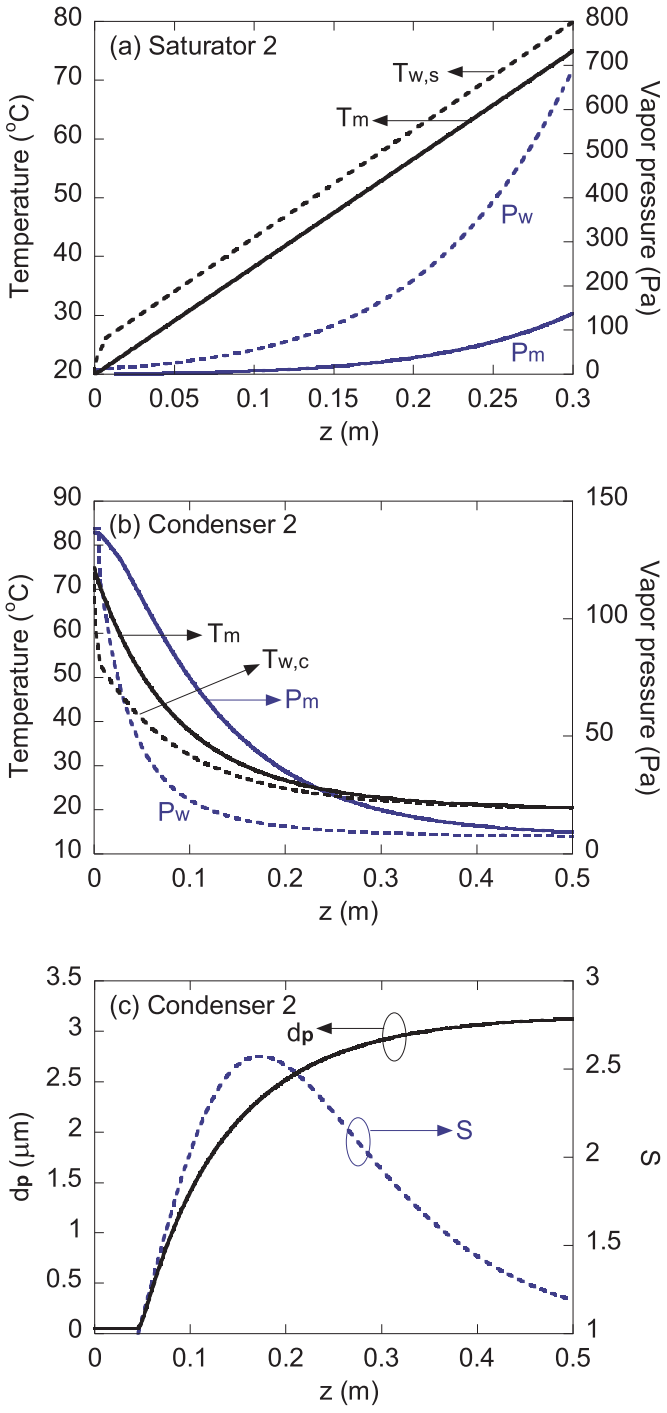

Fig. 7. Model predictions of axial profiles of (a) temperatures of gas and vapor pressures of EG vapor in Saturator 2 (d_s = 1″), (b) temperatures of gas and vapor pressures of EG vapor in Condenser 2 (d_c = ¼"), (c) supersaturation ratio of EG vapor and diameter of growing particles in Condenser 2; T_H = 80 °C, T_L = 20 °C, Q_p = 500 ccm.

3.1 μm, which is smaller than the 3.8 μm in Fig. 6(c). The main reason is that the residence time of the particles in the narrow condenser is four times shorter.

It should be emphasized that the model prediction (3.1 μm) is again in reasonable agreement with the experimental data (~2.8 μm) in Fig. 5. Since Eq. (B10) provides an upper limit of particle growth irrespective of the particle population, this agreement suggests that the present (2nd) design of the particle magnifier works properly for growing Ag particles at the highest concentration.

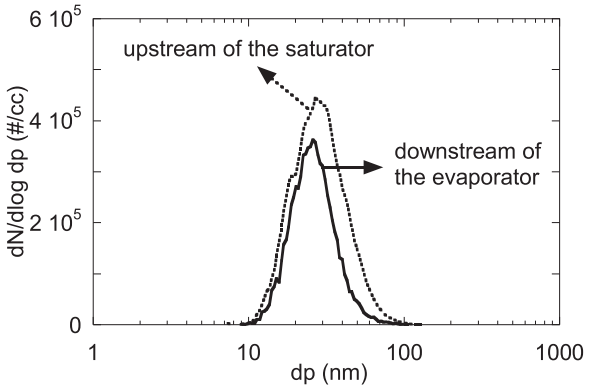

Fig. 8. Comparison of particle size distributions of Ag particles, upstream and downstream of the proposed size-independent charger system; d_s = 1″, d_c = ¼″, T_H = 80 °C, T_L = 20 °C, Q_p = 500 ccm.

3.4. Size-independent charging and production yield of DMA-classified nanoparticles

Half of this section is devoted to evaluating the particle magnifier in conjunction with the corona charger and evaporator as a size-independent charger, and the rest demonstrates its performance for size classification of nanoparticles at high concentrations when combined with DMA.

Fig. 8 compares the size distributions of the Ag nanoparticles measured upstream of the particle magnifier and downstream of the evaporator. After passing through the evaporator, the microdroplets were found to return to their original sizes, which indicates the complete removal of EG from the droplets. The overall transport loss of the nanoparticles through the entire charger system was measured to be less than 20%. Here, since the major loss was confirmed to occur in the corona charger, there are opportunities for further reducing particle loss, e.g., by changing the design to a wire-plate corona charger operating without a sudden change in aerosol flow, separating the aerosol flow from the corona discharge volume, and/or applying AC voltage to minimize the electrostatic loss of particles (Intra & Tippayawong, 2011).

The NaCl nanoparticles seen in Fig. 4(b) were first classified into 20, 30, 40 nm by a DMA and then fed into the size-independent charger. The mean charge number (n_c) and extrinsic charging efficiency (η_c) were then measured for each size of classified particles (refer to Section 2.2 with Eqs. (2) and (3)).

Fig. 9 demonstrates that the proposed charger was indeed able to achieve size-independent charging. The charge number and charging efficiency were both fairly constant in the size range of 20–40 nm; n_c = 32.4 ± 1.1 and η_c = 52 ± 1%. It is notable that the extrinsic charging efficiency is 7–4 times higher than the value (8–14% at 20–40 nm) attained with a bipolar charger, respectively (Jiang et al., 2014). Another thing to note is that the degree of improvement in charging efficiency versus the bipolar charger sharply increases when the size of the target particles is reduced. Thus, the proposed charger is expected to be more beneficial for smaller (sub-10 nm) particles.

The DMA-classification experiment was performed for Ag nanoparticles in accordance with the procedure stated in Section 2.3. DMA voltage was adjusted differently at a target size of 14.5 nm, considering the difference in the charge numbers of the particles (+32 for the proposed charger vs +1 for the bipolar charger).

In Fig. 10, the size distribution of the size-selected particles with the proposed charger was compared with that obtained with the

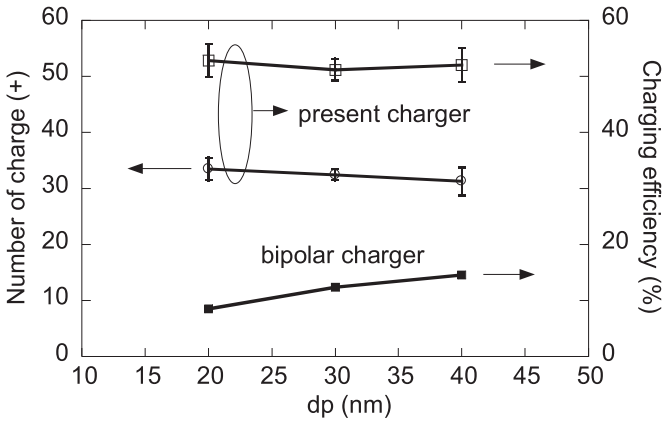

Fig. 9. Demonstration of the size-independent charging of size-selected NaCl nanoparticles using the proposed size-independent charger; d_s = 1″, d_c = ¼″, T_H = 80 °C, T_L = 20 °C, Q_p = 500 ccm.

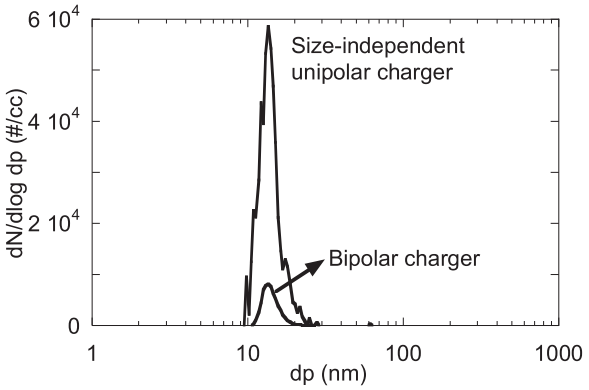

Fig. 10. The size-classification performance of DMA equipped with the proposed size-independent charger, compared with that of a bipolar charger at a Ag particle target size of of 14.5 nm; the operating conditions of the particle magnifier were d_s = 1″, d_c = ¼″, T_H = 80 °C, T_L = 20 °C, Q_p = 500 ccm.

bipolar charger. It is clearly demonstrated that the DMA becomes more powerful with the size-independent charger. The total number concentration of classified particles reached 8250 # cm^{-3}, in contrast to 1010 # cm^{-3} in the case of the bipolar charger. Here, the total number concentration represents the CPC indication (N_1) for the particles which passed through the first DMA (DMA_1). The GSD of the classified particles using the proposed charger was 1.181, slightly larger than the 1.175 for the bipolar charger. In addition, the mode diameters of particles classified at 14.5 nm in both cases were about the same, around 14.0 nm. This implies that the charge number (+32) can be extended down to 14.5 nm, beyond the size range in Fig. 9, with which the DMA is working.

Stolzenburg and McMurry (2008) presented an approximated equation for relating the N_1 to the transfer function of DMA_1 and other parameters of the key components (charger, DMA_1 and CPC) as follows.

$$N_1(V_1) = \eta_{CPC}(d_{p1}^*)\eta_c(d_{p1}^*)\frac{dN}{dlogd_{p1}}\Big|_{d_{p1}^*}\frac{\beta_1(1+\delta_1)}{a_1^*}; a_1^* = -\frac{dlogZ_{p1}}{dlogd_{p1}}, \tag{4}$$

where η_{CPC} is the counting efficiency (~84% at $d_{p1}{}^* = 14.5$ nm) of the CPC, and η_c is the extrinsic charging efficiency of the charger (52% for the proposed charger vs 5.7% for bipolar charger from Jiang et al., 2014). Since DMA_1 operates with a sheath to aerosol flow ratio of 10:1 (refer to Section 2.3), we obtained $\beta_1 = 0.1$ & $\delta_1 = 0$ irrespective of charger types. Given $dN/dlogd_{p1}$ (~445,000 # cm^{-3}) at $d_{p1}{}^* = 14.5$ nm from Fig. 5 & the η_c of the bipolar charger, N_1 is now calculated to 1090 # cm^{-3} which is very close to the measured value (1010 # cm^{-3}).

This calculation was repeated for the proposed charger system by substituting the value of 52% into the η_c in Eq. (4), yielding N_1 = 9900 # cm^{-3} which is 20% higher than the experimental data (8250 # cm^{-3}). This seems to indicate that there is an additional 20% loss of particles. Nevertheless, the 8.2-fold increase in the yield of monodisperse particles was in reasonable agreement with the 9.1-fold increase from the theory. Since the performance improvement was achieved with no change but the charger, it can be concluded that the yield increase was caused by the charger improvement.

In addition, it is noted that the proposed size-independent charger can be used in combination with previous methods that have been proposed to improve the productivity of monodisperse nanoparticles using DMA (Bezantakos et al., 2016; Hontanon & Kruis, 2009), as well as with any improved design of unipolar chargers (Intra & Tippayawong, 2011; Qi, Chen, & Pui, 2007).

The nanoparticles classified using the proposed charger were further tested to assess their monodispersity using a transmission electron microscope (TEM). The charged monodisperse particles from DMA_1 with the proposed charger were electrophoretically deposited on a TEM grid and their TEM image is shown in Fig. 11(a). The bar represents 100 nm, and the inset figure is a magnified image of the particles. Image analysis was performed to determine their size distribution under normalization. Fig. 11(b) shows that the result was again in reasonable agreement with the SMPS result in Fig. 10.

4. Conclusion

In this study, a novel approach was proposed to improve the yield of size-selected monodispersed nanoparticles using DMA. The key idea was to combine the condensational growth of nanoparticles with the efficient charging of unipolar chargers. Based on the nature of vapor condensation, which can cause growing particles to become monodisperse in size, a series of preliminary studies were performed, leading to the unique design of a size-independent unipolar charger, consisting of a porous alumina-lined saturator tube with heater, an air-cooled condenser tube, a fin-cone corona charger, and an evaporating tube. Employing ethylene glycol as a condensing vapor, polydisperse 65-nm NaCl and 20-nm Ag particles were successfully grown to a few micrometers in a second, with a geometric standard deviation below 1.20. A simple model was also developed to explain the heat and mass transfer occurring in the saturator and condenser, and the model successfully predicted the particle growth. As a result, the size-independent unipolar charging was experimentally proven using a subsequent regular corona charger. The produced particles were charged up to + 32 elemental charges, with an extrinsic charging efficiency of ~52%, irrespective of their sizes. A DMA was subsequently used to classify

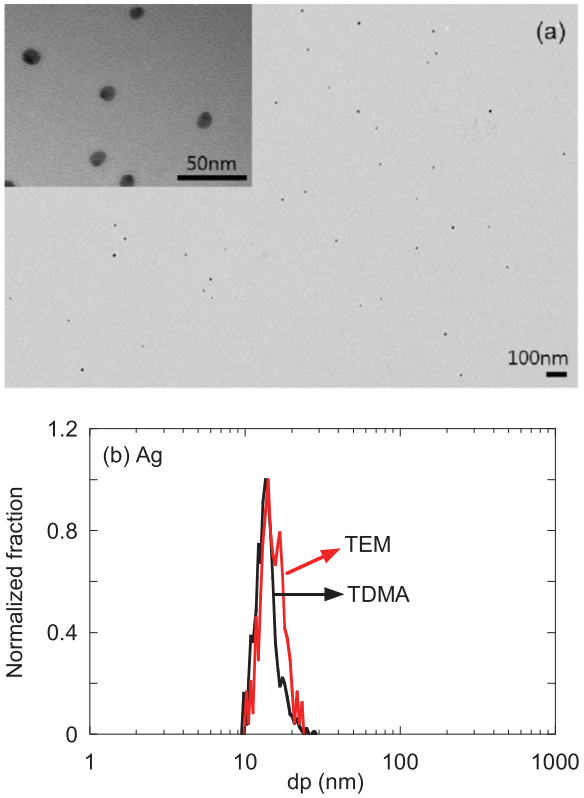

Fig. 11. (a) TEM image of the Ag nanoparticles classified at 14.5 nm with the (proposed) charger-installed nano DMA, (b) comparison of the nanoparticle size distribution from the image analysis, with that from the TDMA measurement in Fig. 10.

the Ag particles at a target size of 14.5 nm, resulting in an 8.2-fold increase in the production yield of classified monodisperse particles.

Acknowledgement

This work was supported by the National Research Foundation of Korea for research numbers of No. 2014M3C8A5030614 and No. 2016R1A2B2014141, both of which were funded by the Ministry of Science and ICT, Korea.

Appendix A. Choice of a condensing liquid

Ethylene glycol (EG) was finally selected as the condensing liquid after considering water and EG both of which have been tested as a working fluid in CPC (Kim, Okuyama, & Fernandez de la Mora, 2003). There are two reasons for the choice as follows. First, the condensing liquid must suppress self-nucleation up to high levels of supersaturation so that the particles grow faster only by condensation. Let us suppose that the saturator temperature (T_H) is increased while the temperature of the condenser is held constant at T_L = 20 °C, in an attempt to increase the supersaturation ratio of the vapor (S) and the resulting growth rate of particles by condensation (see Eq. (1)). If the S increases beyond a threshold, homogeneous nucleation of the EG occurs by creating a large number of liquid nuclei, and then initiates rapid interparticle coagulation. Once this happens, the size distribution of the grown particles is not narrowed but widened, approaching a self-preserving size distribution with a GSD of 1.3–1.4 (Kodas & Hampden-Smith, 1999; Vemury & Pratsinis, 1995; Zahaf & Kim, 2015), and eventually causes our approach to fail.

The rate of homogeneous nucleation can be compared for water and EG under the same conditions. Using Eq. (A1) (Kodas & Hampden smith, 1999; Moon & Lee, 2013), the nucleation rate was calculated at T_H = 50 °C & T_L = 20 °C using Eq. (A1). As a result, the nucleation rate of EG was four orders of magnitude lower than that of water (0.045 vs 571.3 # $cm^{-3}\,s^{-1}$). This is attributed to the fact that the heavier EG is less volatile than water by two orders of magnitude, lowering the saturation vapor pressure (P_{EG}) and number density (N_{EG}) of vapor in Eq. (A1) (P_{EG} = 94 Pa vs P_{H2O} = 12,325 Pa at T_H). This implies that EG was not sensitive to the temperature difference between the saturator and condenser ($\Delta T = T_H - T_L$) compared to water, which allows a margin for uncertainties in the temperature control of the system.

$$J = \frac{P_{EG}}{k_B T\sqrt{2\pi m_{EG}}} 2\nu_{EG}\sigma_{EG}^{1/2} N_{EG} \exp\left[-\frac{16\pi}{3}\frac{\nu_{EG}^2\sigma_{EG}^3}{(k_B T)^3(lnS)^2}\right], \tag{A1}$$

where m_{EG} and ν_{EG} are the molecular mass and volume of the condensing vapor, respectively, σ_{EG} is the surface tension of the condensed phase, and k_B is the Boltzmann constant.

The second reason for the choice was that EG is better than water in terms of heat and mass transfer in the condenser. It is worth noting that the mass diffusivity of water vapor ($Dv_{,H2O} = 0.24\,cm^2\,s^{-1}$) is slightly greater than the thermal diffusivity of the carrier gas ($\alpha = 0.21\,cm^2\,s^{-1}$), while EG has a much lower mass diffusivity of $D_{EG} = 0.039\,cm^2\,s^{-1}$. This means that water vapor diffuses to the condenser wall as fast as heat transfers from the carrier gas to the wall (Hering & Stolzenburg, 2005). As a result, water vapor is mostly condensed onto the wall rather than onto the particles, particularly in the entrance region of the condenser where the carrier gas is cooled down to the wall temperature. On the other hand, the less mobile EG vapor preserves its initial concentration longer, except near the wall, until the falling gas temperature almost reaches the wall temperature, creating a more uniform concentration field with a higher level of supersaturation. For these reasons, EG was finally selected as the condensing liquid in the present study.

Appendix B. Analysis of heat and mass transfer and particle growth in the saturator and condenser

Since the monodispersity of grown droplets is primarily determined by the local variation in the supersaturation ratios of EG vapor, the heat and mass transfer occurring in the alumina-lined saturator and condenser, as well as the resulting particle growth, were analyzed by developing a simple model. This section describes the model derivation in detail.

As described in Section 2.2, the saturator tube was heated by a heating tape. Assuming that a uniform heat flux (q_s") was given to the wall of the saturator tube, the convective heat transfer coefficient ($h_{i,s}$) can be calculated as a function of axial distance (z) from the inlet of the saturator using Eq. (B1) (Middleman, 1998).

$$\begin{cases} Nu_{ds} = \frac{h_{i,s}d_s}{k_g} = 1.076(z^*)^{-\frac{1}{3}} \;\; for \;\; z^* = \frac{z/d_s}{PrRe_{ds}} < 0.01 \\ \qquad Nu_{ds} = 4.36 \;\; for \;\; z^* \geq 0.01 \end{cases}, \tag{B1}$$

where Pr is the Prandtl number of the gas, k_g is the heat conductivity of the gas, and Nu_{ds} and Re_{ds} are the Nusselt number and Reynolds number, both of which are defined based on d_s (the diameter of the saturator tube) respectively. The mean velocity (U) used for the calculation of Re_{ds} is calculated from the volume flow rate ($Q = 0.5$ lpm) of the carrier gas measured at room temperature, as well as the d_s here or d_c for the condenser later. The two equations in Eq. (B1) illustrate the well-known fact that the $h_{i,s}$ gradually decreases along the distance z and reaches a constant value at $z^* = 0.01$ where the thermal boundary layer is fully developed.

The energy balance model in the tube (Incropera et al., 2007) was used to calculate the cup-mixing temperature of the gas ($T_m(z)$) and wall temperature of the tube ($T_{w,s}(z)$) as seen in Eqs. (B2) and (B3), respectively.

$$T_m(z) = T_{m,i} + \frac{q_s^{"}\pi d_s}{\rho_g Q C_p} z \tag{B2}$$

$$T_{w,s}(z) = T_m(z) + \frac{q_s^{"}}{h_{i,s}(z)} \tag{B3}$$

Here, ρ_g and C_p are the average density and heat capacity of the gas, and $T_{m,i}$ is the inlet temperature of the gas (20 °C) at $z = 0$. As addressed in Section 2.2, the saturator temperature T_H was defined as the wall temperature measured at the exit of the saturator. To reflect this, the q_s" was adjusted to achieve $T_{w,s}(L_s) = T_H$ by combining Eqs. (B2) and (B3).

Likewise, a local convective mass transfer coefficient ($h_{m,s}(z)$) was calculated in the developing and fully developed region using the corresponding Sherwood number correlations:

$$\begin{cases} Sh_{ds} = \frac{h_{m,s}d_s}{D_{EG}} = 1.076(z^*)^{-\frac{1}{3}} \;\; for \;\; z^* = \frac{z/d_s}{ScRe_{ds}} < 0.01 \\ \qquad Sh_{ds} = \frac{3.66+4.36}{2}\left(\frac{Sc}{Pr}\right)^{1/3} \;\; for \;\; z^* \geq 0.01 \end{cases}, \tag{B4}$$

where Sc is the Schmidt number (ν/D_{EG}) where ν is the kinematic viscosity of the gas, Sh_{ds} is the Sherwood number based on d_s, and the other variables are the same as defined earlier. It should be noted that Eq. (B4) was derived by applying the well-known Reynolds analogy (Incropera et al., 2007; Middleman, 1998) to Eq. (B1). By the way, the concentration of EG at the saturated wall ($P_w \cong P_{sat}$) is not constant but varies with z by the axial variation in $T_{w,s}$. Provided that the real boundary condition lies in between the two limiting boundary conditions of the constant heat flux and the constant surface temperature, the second equation in Eq. (B4) is obtained by taking an average of the corresponding Nusselt numbers (3.66 and 4.36) (Incropera et al., 2007).

A one-dimensional differential equation was derived to achieve an axial profile of the average concentration of EG vapor (C_m) based on the mass balance:

$$\frac{dC_m}{dz} = -\frac{\pi d_s}{Q} h_{m,s}(C_m - C_w), \tag{B5}$$

where C_w is the wall concentration of EG, which is estimated from the saturation vapor pressure P_{sat} at $T_{w,s}$. Since C_w is also a function of z like $T_{w,s}$, Eq. (B5) was numerically integrated to calculate $C_m(z)$ at each z position. Given $T_m(z)$ and $C_m(z)$, the average vapor pressure of EG ($P_m(z)$) is calculated by applying the ideal gas law. These numerical calculations were repeated with a sufficiently small increment of $\Delta z = 0.5$ mm until $z = L_s$. The values of T_m, C_m, and P_m at the exit of the saturator were used as input parameters

for the following analysis for the condenser.

Unlike the saturator, which is heated by a uniform heat flux, the outer surface of the condenser was subject to natural convective cooling at $T_L = T_\infty = 20$ °C. Thus, the internal and external convective heat transfer on both sides of the condenser tube need to be solved simultaneously to determine the surface temperature ($T_{w,c}(z)$) and cup-mixing temperature ($T_m(z)$) of the gas in the condenser. The wall conduction resistance of the tube was neglected for simplicity. Another simple energy balance at steady state was developed for the overall heat transfer from the tube flow to the outer environment through the tube wall. Eq. (B6) shows a general expression that relates the three important thermal variables of T_m, $T_{w,c}$, and T_∞, irrespective of the tube flow conditions.

$$\frac{dT_m(z)}{dz} = -\frac{\pi d_c}{\rho_g Q C_p} h_{i,c}(z)(T_m(z) - T_{w,c}(z)) = -\frac{\pi d_c}{\rho_g Q C_p} h_{o,c}(z)(T_{w,c}(z) - T_\infty) \tag{B6}$$

Equating the two terms on the right-hand side, the $T_{w,c}$ can be expressed in terms of T_m and T_∞ as

$$T_{w,c}(z) = \frac{h_{i,c}(z)T_m(z) + h_{o,c}(z)T_\infty}{h_{i,c}(z) + h_{o,c}(z)} \tag{B7}$$

Here, $h_{i,c}(z)$, the convection heat transfer coefficient on the inner surface, may be calculated by replacing the variables in Eq. (B1) with those of the condenser, except that the average of 3.66 and 4.36 was used instead of 4.36 for a change in surface boundary condition. $h_{o,c}(z)$ represents the natural-convection heat transfer coefficient on the outer tube surface and is calculated by

$$\overline{Nu_{dc}} = \frac{h_{o,c} d_c}{k_g} = \left[0.6 + \frac{0.387 Ra_D^{1/6}}{[1+(0.559/Pr)^{9/16}]^{8/27}}\right]^2 for \;\; Ra_D < 10^{12}, \tag{B8}$$

where Ra_D is the Rayleigh number based on the diameter of the condenser (d_c). (Incropera et al., 2007) The maximum Ra_D in this study was 2650 for d_c = ½" and 595 for d_c = ¼", within the valid range of Ra_D in Eq. (B8). Since Ra_D is linearly proportional to $T_{w,c}(z)$ decreasing with z, the term $h_{o,c}$ also decreases with z.

Substituting Eq. (B7) into Eq. (B6) and integrating, $T_m(z)$ is expressed as

$$\frac{T_m(z) - T_\infty}{T_{m,i} - T_\infty} = exp\left(-\frac{\pi d_c}{\rho_g Q C_p} h(z) \cdot z\right), \tag{B9}$$

where $h(z) = \frac{1}{z}\int_0^z \frac{h_{i,c}(z) h_{o,c}(z)}{h_{i,c}(z) + h_{o,c}(z)} dz$.

Hence, starting from the inlet at $z = 0$, the axial profile of $T_m(z)$ is obtained by repeating the numerical integration for $h(z)$ up to the tube exit. Meanwhile, the wall temperature $T_{w,c}(z)$ is calculated from Eq. (B7) with the obtained $T_m(z)$. With water cooling of the condenser, where $h_{o,c}$ is so large as to be considered infinite ($h_{o,c} \to \infty$), Eq. (B7) is reduced to yield a constant surface temperature ($T_{w,c}(z) \to T_\infty$), as expected.

Mass transfer in the condenser is determined in principle by the same governing equation as in the saturator, except that the evaporation of EG is reversed by condensation. Assuming the wall saturation with EG, $P_w(z)$ ($\cong P_{sat}(T_{w,c})$) and $C_w(z)$ are calculated from the foregoing $T_{w,c}(z)$. The cup-mixing average concentration of EG vapor at the exit of the saturator is now an inlet boundary condition. With these inlet and wall boundary conditions, again Eq. (B5) is numerically integrated to determine $C_m(z)$ and $P_m(z)$ along the z axis, replacing the terms of d_s and $h_{m,s}$ with d_c and $h_{m,c}$.

When nanoparticles enter the condenser, they are often assumed to instantaneously reach a local thermal equilibrium with the surrounding gas owing to their small sizes. Thus, the particle temperature (T_d) was approximated by T_m. Moreover, the condensing surface of the particles was assumed to be saturated, leading to $P_d \cong P_{sat}(T_d)$ where P_d is the partial pressure of EG on the surface. While T_m quickly decreases with z along the condenser tube, the C_m or P_m of the EG vapor slowly decreases due to the low mass transfer to the wall. This creates a partial-pressure difference between the particle surface and the surrounding gas (P_m - P_d > 0) so that EG vapor condensation on the particles commences. It is worth noting that the driving force for the condensational growth of particles is P_m - P_d ($\cong P_m - P_{sat}(T_m)$), not P_m - P_w ($\cong P_m - P_{sat}(T_{w,c})$).

Applying these foregoing assumptions, the growth rate of the particles in Eq. (1) is now expressed as

$$\frac{d(d_p)}{dt} = \frac{4 D_{EG} v_{EG} (P_m(z) - P_d) F_2}{k_B T_m d_p}, \quad F_2 = \frac{1+K_n}{1 + 1.7K_n + 1.333K_n^2}, \quad P_d \approx P_{sat}(T_m), \tag{B10}$$

where K_n is the Knudsen number. Assuming a steady-state incompressible gas flow, the time derivative $d(d_p)/dt$ may be expressed as $Ud(d_p)/dz$ where U is the mean velocity of the carrier gas. This allows the numerical integration of two ordinary differential equations (Eqs. (B5) and (B10)) combined with two analytic solutions (Eqs. (B7) and (B9)) against z, starting from the inlet to the outlet of the condenser. Meanwhile, the particles' temperature may be increased during vapor condensation by the latent heat of condensation, but this effect was found to be negligible for all conditions we considered.

References

Anantha, P., Cheng, T., Tay, Y. Y., Wong, C. C., & Ramanujan, R. V. (2015). Facile production of monodisperse nanoparticles on a liquid surface. *Nanoscale, 7*, 16812–16822.

Bezantakos, S., Giamarelou, M., Huang, L., Olfert, J., & Biskos, G. (2016). Modification of the TSI 3081 differential mobility analyzer to include three monodisperse outlets: Comparison between experimental and theoretical performance. *Aerosol Science and Technology, 50*, 1342–1351.
Birmili, W., Stratmann, F., Wiedensohler, A., Covert, D., Russel, L. M., & Berg, O. (1997). Determination of differential mobility analyzer transfer functions using identical instruments in series. *Aerosol Science and Technology, 27*, 215–223.
Chen, D.-R., Pui, D. Y. H., Hummes, D., Fissan, H., Quant, F. R., & Sem, G. J. (1998). Design and evaluation of a nanometer aerosol (nano-DMA). *Journal of Aerosol Science, 29*, 497–509.
Choi, Y., & Kim, S. (2007). An improved method for charging submicron and nano particles with uniform charging performance. *Aerosol Science and Technology, 41*, 259–265.
Domat, M., Kruis, F. E., & Fernandez-Diaz, J. M. (2014). Investigations of the effect of electrode gap on the performance of a corona charger having separated corona and charging zones. *Journal of Aerosol Science, 68*, 1–13.
Hering, S. V., & Stolzenburg, M. R. (2005). A method for particle size amplification by water condensation in a laminar, thermally diffusive flow. *Aerosol Science and Technology, 39*, 428–436.
Hinds, W. C. (1999). *Aerosol technology: Properties, behavior, and measurement of airborne particles (Chapters 13, 15)* (2nd ed.). New York: John Wiley & Sons.
Hewitt, G. W. (1957). The charging of small particles for electrostatic precipitation. *IEEE Transactions on Communications, 76*, 300–306.
Hontanon, E., & Kruis, F. E. (2009). A differential mobility analyzer (DMA) for size selection of nanoparticles at high flow rates. *Aerosol Science and Technology, 43*, 23–37.
Incropera, F. P., Dewitt, D. P., Bergman, T. L., & Lavine, A. S. (2007). *Introduction to heat transfer (Chapters 6, 8, 9)* (5th ed.). USA: John Wiley & Sons.
Intra, P., & Tippayawong, N. (2011). An overview of unipolar charger developments for nanoparticle charging. *Aerosol and Air Quality Research, 11*, 187–209.
Jiang, J., Kim, C., Wang, X., Stolzenburg, M. R., Kaufman, S. L., Qi, C., ... McMurry, P. H. (2014). Aerosol charge fractions downstream of six bipolar chargers: Effects of ion source, source activity, and flowrate. *Aerosol Science and Technology, 48*, 1207–1216.
Kim, D. S., Lee, D. S., Woo, C. G., & Choi, M. (2006). Control of nanoparticle charge via condensation magnification. *Journal of Aerosol Science, 37*, 1876–1882.
Kim, C. S., Okuyama, K., & Fernandez de la Mora, J. (2003). Performance evaluation of an improved particle size magnifier (PSM) for single nanoparticle detection. *Aerosol Science and Technology, 37*, 1–13.
Kodas, T. T., & Hampden-Smith, M. J. (1999). *Aerosol processing of materials (Chapters 4, 5)*. New York: Wiley-VCH.
Kousaka, Y., Okuyama, K., & Adachi, M. (1985). Determination of particle size distribution of ultra-fine aerosols using a differential mobility analyzer. *Aerosol Science and Technology, 4*, 209–225.
Knutson, E. O., & Whitby, K. T. (1975). Aerosol classification by electric mobility: Apparatus, theory, and applications. *Journal of Aerosol Science, 6*, 443–451.
Kruis, F. E., Fissan, H., & Peled, A. (1998). Synthesis of nanoparticles in the gas phase for electronic, optical and magnetic applications-a review. *Journal of Aerosol Science, 296*, 511–535.
Lee, D., & Choi, M. (2002). Coalescence enhanced synthesis of nanoparticles to control size, morphology and crystalline phase at high concentrations. *Journal of Aerosol Science, 33*, 1–16.
Lee, D., Park, K., & Zachariah, M. R. (2005). Determination of the size distribution of polydisperse nanoparticles with single-particle mass spectrometry: The role of ion kinetic energy. *Aerosol Science and Technology, 39*, 162–169.
Lee, H., You, S., Pikhitsa, P. V., Kim, J., Kwon, S., Woo, C. G., & Choi, M. (2011). Three-dimensional Assembly of nanoparticles from charged aerosols. *Nano Letters, 11*, 119–124.
Lee, H., Kim, T. J., Li, C., Choi, I. D., Kim, Y. T., Coker, Z., & Lee, D. (2014). Flame aerosol synthesis of carbon-supported Pt-Ru catalysts for a fuel cell electrode. *International Journal of Hydrogen Energy, 39*, 14416–14420.
Lee, K. S., Hwang, T. H., Kim, S.-H., Kim, S. H., & Lee, D. (2013). Numerical simulations on aerodynamic focusing of particles in a wide size range of 30 nm–10 μm. *Aerosol Science and Technology, 47(9)*, 1001–1008.
Lüönd, F., & Schlatter, J. (2013). Improved monodispersity of size selected aerosol particles with a new charging and selection scheme for tandem DMA setup. *Journal of Aerosol Science, 62*, 40–55.
Liu, H., Song, C., Zhang, L., Zhang, J., Wang, H., & Wilkinson, D. P. (2006). A review of anode catalysis in the direct methanol fuel cell. *Journal of Power Sources, 155*, 95–110.
Middleman, S. (1998). *An introduction to mass and heat transfer: Principles of analysis and design (Chapters 6, 12)* (1st ed.). New York: John Wiley & Sons.
Moon, B.-J., & Lee, D. (2013). Understanding morphology-controlled synthesis of zinc nanoparticles and their characteristics of hydrolysis reaction. *Langmuir, 29*, 6174–6180.
Pyo, J., Ock, Y., Jeong, D., Park, K., & Lee, D. (2017). Development of filter-free particle filtration unit utilizing condensational growth: With special emphasis on high-concentration of ultrafine particles. *Building and Environment, 112*, 200–208.
Qi, C., Chen, D.-R., & Pui, D. Y. H. (2007). Experimental study of a new corona-based unipolar aerosol charger. *Journal of Aerosol Science, 38*, 775–792.
Rader, D. J., & McMurry, P. H. (1986). Application of the tandem differential mobility analyzer to studies of droplet growth or evaporation. *Journal of Aerosol Science, 17*, 771–787.
Stolzenburg, M. R., & McMurry, P. H. (2008). Equations governing single and tandem DMA configurations and a new lognormal approximation to the transfer function. *Aerosol Science and Technology, 42*, 421–432.
Suh, J., Han, B., Kim, D. S., & Choi, M. (2005). A method for enhanced charging of nanoparticles via condensation magnification. *Journal of Aerosol Science, 36*, 1183–1193.
Vemury, S., & Pratsinis, S. E. (1995). Self-preserving size distributions of agglomerates. *Journal of Aerosol Science, 26*, 175–185.
Vivas, M. M., Hontanon, & Schmidt-Ott, A. (2008). Reducing multiple charging of submicron aerosols in a corona diffusion charger. *Aerosol Science and Technology, 42*, 97–109.
Wang, X. W., Zhong, H. H., & Snyder, R. L. (1990). Rf plasma aerosol deposition of superconductive $Y_1Ba_2Cu_3O_{7-\delta}$ films at atmospheric pressure. *Applied Physics Letters, 57*, 1581–1583.
Yook, S.-J., Fissan, H., Engelke, T., Asbach, C., v. d. Zwaag, T., Kim, J. H., ... Pui, D. Y. H. (2008). Classification of highly monodisperse nanoparticles of NIST-traceable sizes by TDMA and control of deposition spot size on a surface by electrophoresis. *Journal of Aerosol Science, 39*, 537–548.
Zahaf, R., Kim, S. K., Shin, J., Park, K., Choi, T.-Y., & Lee, D. (2015). Effect of volume fraction on transient structural behavior of aerosol particles using off-lattice kinetic Monte Carlo simulation. *Aerosol Science and Technology, 49*, 1242–1255.
Zeng, S., Yu, X., Law, W.-C., Zhang, Y., Hu, R., Dinh, X.-Q., & Yong, K.-T. (2013). Size dependence of Au NP-enhanced surface plasmon resonance based on differential phase measurement. *Sensors & Actuators, B: Chemical, 176*, 1128–1133.